

# **Simulating the Fracture of Notched Mortar Beams through Extended Finite Element Method (XFEM) and Peridynamics**

Sumanta Das, Canio Hoffarth, Bo Ren,  
Benjamin Spencer, Gaurav Sant,  
Subramanian D. Rajan, Narayanan  
Neithalath

May 2019



The INL is a U.S. Department of Energy National Laboratory  
operated by Battelle Energy Alliance

# **Simulating the Fracture of Notched Mortar Beams through Extended Finite Element Method (XFEM) and Peridynamics**

**Sumanta Das, Canio Hoffarth, Bo Ren, Benjamin Spencer, Gaurav Sant,  
Subramanian D. Rajan, Narayanan Neithalath**

**May 2019**

**Idaho National Laboratory  
Idaho Falls, Idaho 83415**

**<http://www.inl.gov>**

**Prepared for the  
U.S. Department of Energy**

**Under DOE Idaho Operations Office  
Contract DE-AC07-05ID14517**

# Simulating the Fracture of Notched Mortar Beams through Extended Finite Element Method (XFEM) and Peridynamics

Sumanta Das<sup>1,\*</sup>, Canio Hoffarth<sup>2</sup>, Bo Ren<sup>3</sup>, Benjamin Spencer<sup>4</sup>, Gaurav Sant<sup>5</sup>, Subramaniam D. Rajan<sup>2</sup>, Narayanan Neithalath<sup>2</sup>

<sup>1</sup>Department of Civil and Environmental Engineering, University of Rhode Island, Kingston, RI, USA

<sup>2</sup>School of Sustainable Engineering and the Built Environment, Arizona State University, Tempe, AZ, USA.

<sup>3</sup>Livermore Software Technology Corporation, Livermore, California, USA

<sup>4</sup>Fuels Modeling and Simulation, Idaho National Laboratory, Idaho Falls, ID, USA

<sup>5</sup>Departments of Civil and Environmental Engineering and Materials Science and Engineering, University of California Los Angeles, Los Angeles, CA, USA

\*Corresponding author: Sumanta Das ([sumanta\\_das@uri.edu](mailto:sumanta_das@uri.edu))

*Das Sumanta, Hoffarth Canio, Ren Bo, Spencer Benjamin, Sant Gaurav, Rajan Subramaniam D., Neithalath Narayanan, Simulating the Fracture of Notched Mortar Beams through Extended Finite-Element Method and Peridynamics, J. Eng. Mech. 145 (2019) 04019049. doi:10.1061/(ASCE)EM.1943-7889.0001628.*

Final version available at:

[https://doi.org/10.1061/\(ASCE\)EM.1943-7889.0001628](https://doi.org/10.1061/(ASCE)EM.1943-7889.0001628)

## ABSTRACT

This paper simulates fracture in notched mortar beams under three-point bending using extended finite element method (XFEM) and peridynamics. A three-phase microstructure (i.e., cement paste, aggregates, and paste-aggregate interface) is used for constitutive modeling of the mortar to obtain the elastic properties for simulation. In the XFEM approach, the simulated homogenized elastic modulus is used along with the total fracture energy of the cement mortar in a damage model to predict the fracture response of the mortar including crack propagation and its fracture parameters (Mode I stress intensity factor,  $K_{IC}$  and critical crack tip opening displacement,  $CTOD_C$ ). The damage model incorporates a maximum principal stress-based damage initiation criteria and a traction-separation law for damage evolution. In the peridynamics approach, a bond-based model involving a prototype microelastic brittle (PMB) material model is used. The elastic properties and fracture energy release rates are used as inputs in the PMB model, along with the choice of peridynamic horizon size. Comparison with experimental fracture properties ( $K_{IC}$ ,  $CTOD_C$ ) as well as crack propagation paths from digital image correlation show that both the approaches yield satisfactory results, particularly for  $K_{IC}$  and crack extension. Thus, both these methods can be adopted for fracture simulation of cement-based materials.

**Keywords:** Numerical simulation; Fracture; Constitutive model; XFEM; Peridynamics; Concrete

## 1. INTRODUCTION

Rapid progress is noted in the development and application of novel and sustainable binders as well as several types of inclusions (both stiff and compliant) for structural concrete applications. In the binder domain, high volume cement replacement materials and cement-free binders (e.g., alkali activated binders) are gaining prominence (Das et al. 2014b; Juenger et al. 2011; Ravikumar et al. 2010). The use of lightweight aggregates (LWAs) are being explored for internal curing and thermal and acoustic insulation (Al-Jabri et al. 2005; Cusson and Hoogeveen 2008; Kim et al. 2012; Nguyen et al. 2014). In addition, microencapsulated phase change materials (PCMs) are being proposed for control of thermal cracking in pavements and bridge decks (Fernandes et al. 2014), and regulating internal environments in buildings (Hembade et al. 2013; Thiele et al. 2015), while soft inclusions such as rubber are used for energy absorption (Hernández-Olivares et al. 2002), and denser/stiffer aggregates for radiation shielding (Akkurt et al. 2006; Makarios et al. 1996). The changes in the binder phase and/or incorporation of novel inclusions influence the microstructural stress distribution and consequently the paths/mode of failure of the material (Das et al. 2016a). The bulk fracture response of these systems are thus dictated by the microstructure, even though macroscale descriptors are often used as fracture parameters.

Numerical simulations of mechanical and fracture response of heterogeneous materials such as concrete complement the experimental studies to aid in material selection and optimizing proportions as well as in elucidating the mechanisms of failure. The microstructure-dependent elastic modulus is extracted in this study using a finite element (FE)-based micromechanical modeling scheme. This approach eliminates the shortcomings of typical analytical schemes (Das et al. 2015b; Hori and Nemat-Nasser 1993; Mori and Tanaka 1973) and yields a better solution. The modifications in the binder (paste) phase and the changes in inclusion properties can thus be adequately captured (Das et al. 2016a). The constitutive response thus generated and the experimentally obtained fracture energy data is used to predict crack propagation in macro-scale cementitious mortar beams. Several approaches are available to simulate fracture in cementitious materials, including those based on FE methods (Bobiński and Tejchman 2016; Ren et al. 2017; Sancho et al. 2007) and lattice models (Bolander and Sukumar 2005; Qian and Schlangen 2013). FE models employing the cohesive zone approach (Park et al. 2010; Roesler et al. 2007; Song et al. 2006) have been often studied. The fact that crack paths are highly sensitive to mesh alignment and refinement in a FE model has led to the use of extended finite element method (XFEM), where local enrichment functions with additional degrees of freedom are included in the standard FE approach (Eftekhari et al. 2014; Golewski et al. 2012). Recently, peridynamics has evolved

as a modeling approach for solids with discontinuities (Silling 2000). Here, crack initiation and propagation are represented through bonds between particles. This paper adopts XFEM and bond-based peridynamics along with the elastic modulus predicted from the microstructural analysis to simulate the mesoscale fracture response, including the fracture parameters and crack paths in mortar beams.

## 2. MICROSTRUCTURE-GUIDED MODELING OF ELASTIC PROPERTIES

This section describes the microstructure-guided constitutive modeling framework for cement mortar. The linear constitutive response of cement mortar predicted in this section through microstructural stress analysis is used later as an input to the homogenized damage model for prediction of fracture properties.

### 2.1 Elastic Properties of Component Phases

The constitutive relationships for all the components of the mortar: cement paste, quartz aggregates and the paste-inclusion interface are considered in their respective linear elastic regimes so as to obtain the effective Young's modulus. The default elastic properties of the components, extracted from available literature (Grondin and Matallah 2014; Hashin and Monteiro 2002; Ke et al. 2009; Lutz et al. 1997; Nilsen et al. 1995; Yang 1998; Zanjani Zadeh and Bobko 2014), are presented in Table 1.

Table 1. Elastic properties of the components of the mortar for FE simulations

| Elastic property         | Component phases      |                  |                               |
|--------------------------|-----------------------|------------------|-------------------------------|
|                          | Hardened Cement paste | Quartz inclusion | Quartz-cement paste interface |
| Young's Modulus, E (GPa) | 20                    | 70               | 15                            |
| Poisson's Ratio (–)      | 0.22                  | 0.17             | 0.22                          |

### 2.2 Effective Elastic Property Prediction

This section describes the numerical simulation framework for prediction of effective Young's modulus of cement mortar. The effective Young's modulus of cement mortar is obtained in a three-step process - (1) generation of a unit cell or representative volume element (RVE) based on known inclusion size distributions, (2) meshing of the unit cell and application of appropriate boundary conditions, and (3) microstructural stress analysis.

The RVE is generated using the Lubachhevsky-Stillinger algorithm (Lubachevsky 1991; Lubachevsky et al. 1991; Lubachevsky and Stillinger 1990; Meier et al. 2008), which employs a hard, non-overlapping

particle model in a cubical RVE. The desired number of particles (having an initial radius of zero) are randomly distributed inside the periodic bounding box with random initial velocities of the particles. The radius of  $i^{\text{th}}$  particle ( $r_i$ ) in the next event is a function of growth rate ( $g_i$ ) such that:

$$\frac{dr_i}{dt} = g_i \quad (1)$$

The growth rate of different particles is controlled so as to attain the desired particle size distribution, and is computed using finite difference scheme as follows:

$$g_i = \frac{(r_i^{n+1} - r_i^n)}{\Delta t} \quad (2)$$

The particle radii are updated using the growth rate and time increment. The position of particle 'i' is updated considering a constant velocity between the time nodes as:

$$x_i^{n+1} = x_i^n + v_i^n \Delta t \quad (3)$$

All the particle positions  $x_i^{n+1}$  are updated using forward Euler scheme as shown in Equation 3 and a new search for next collision is started. The post-contact velocities are computed as follows:

$$v_{n_i}^{n+1+} = \min\{v_{n_i}^{n+1-}, v_{n_j}^{n+1-}\} - g_i \quad (4a)$$

$$v_{n_j}^{n+1+} = \max\{v_{n_i}^{n+1-}, v_{n_j}^{n+1-}\} + g_i \quad (4b)$$

During each time step, checks for particle contacts and post-contact velocities are made. These steps are repeated, and in this process, the particles change their position in the RVE, collide, and grow to attain the desired volume fraction.

In the current work, the RVE is generated based on a uniform particle size of 0.6 mm although the microstructure generation algorithm can handle any type of particle size distribution. Once the RVE geometry is generated, periodic boundary conditions (Das et al. 2016b; a; Li 2008; van der Sluis et al. 2000; Xia et al. 2006) are employed in the representative volume element (RVE) as shown in Figure 1. Periodic boundary conditions make the RVE-based approach beneficial as they minimize the boundary effects and stress concentrations near the edges of RVE while using a small problem domain. Figure 1(a) shows periodic arrays of repetitive unit cells and Figure 1(b) shows the periodic boundary conditions applied on a typical unit cell. The periodic boundary conditions ensure two continuity criteria – displacement continuity and traction continuity, at the boundaries of neighboring unit cells (Suquet

1987). The former ensures that the neighboring unit cells cannot be separated or they cannot penetrate each other and the latter implies that traction distributions at the opposite parallel boundaries of the RVE must be the same. The displacement field in the periodic microstructure is given as:

$$v_i(x_1, x_2) = \varepsilon_{ij}^0 x_j + v_i^*(x_1, x_2) \quad (5)$$

where  $\varepsilon_{ij}^0$  is the applied strain tensor, and  $v_i^*$  is a periodic function representing the modification of linear displacement field due to the heterogeneous microstructure.

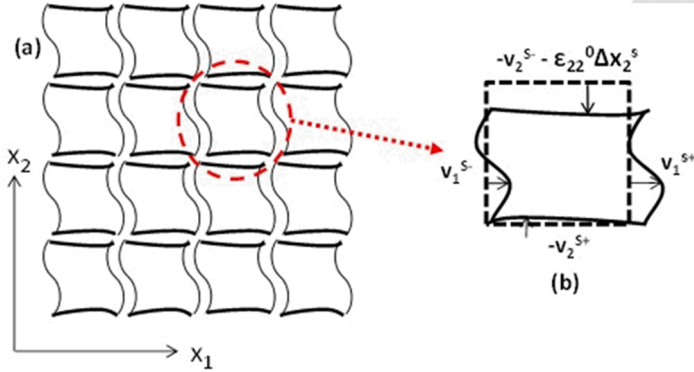


Figure 1: Schematic of the RVEs with periodic boundary conditions under applied strain ( $\varepsilon_{22}^0$ ) (Das et al. 2016a; Suquet 1987).

For the unit cell shown in Figure 1(b), the displacements on a pair of parallel opposite boundary edges are given as:

$$v_i^{s+} = \varepsilon_{ij}^0 x_j^{s+} + v_i^* \quad (6a)$$

$$v_i^{s-} = \varepsilon_{ij}^0 x_j^{s-} + v_i^* \quad (6b)$$

Here,  $s^+$  and  $s^-$  are  $s^{\text{th}}$  pair of two opposite parallel boundary surfaces of the unit cell as shown in Figure 1(b). The periodic function  $v^*$  is the same for both the parallel opposite edges due to periodicity. The difference between the displacement fields of the two opposite parallel boundary edges is given as:

$$v_i^{s+} - v_i^{s-} = \varepsilon_{ij}^0 (x_j^{s+} - x_j^{s-}) = \varepsilon_{ij}^0 \Delta x_j^s \quad (7)$$

For a pair of opposite parallel boundary edges,  $\Delta x_j^i$  is constant for a specified  $\varepsilon_{ij}^0$ . Such equations are applied as nodal displacement constraints in the FE analysis. A specific strain is applied on the RVE and the analysis is implemented through ABAQUS<sup>TM</sup> solver. Thus this approach simulates a strain- (or displacement) controlled test scenario.

To facilitate construction of the FE model, a Python script is used to create the input for ABAQUS<sup>TM</sup> to mesh the RVE and to create the appropriate boundary conditions, thus creating a complete FE model. Free quad-dominated 4-noded bilinear plane strain quadrilateral elements (CPE4R element implemented in ABAQUS<sup>TM</sup>) are used in the FE models. A homogenization module is developed to obtain effective (averaged) RVE stresses/strains. A concurrent mesh convergence study determined that for an RVE 4.15 mm in size, a seed size of 0.0175 mm yielded converging responses. Figure 2(a) shows a representative 2D periodic microstructure (showing all particles of uniform size; please see (Das et al. 2016b) for the same algorithm in which a broader particle size distribution is simulated, in both 2D and 3D). The inclusion volume fraction is 50%. Figure 2(b) shows the stress distributions obtained after analysis under the application of an imposed strain of 0.12% (which is well within the linear elastic range of cementitious systems) in microstructures containing a stiff inclusion (i.e., quartz). In order to determine the Young's modulus, the microstructural stress analysis is performed for different externally applied strains (up to 0.25%). The stress-strain response thus generated through numerical simulation is shown in Figure 2(c). The elastic modulus obtained for the mortar with quartz inclusions is 31.4 GPa, and this value is used in the fracture simulations reported later in this paper. The obtained homogenized Young's modulus correlates well with the values generally reported for mortars containing quartz sand (Yang 1998), as well as our experiments.

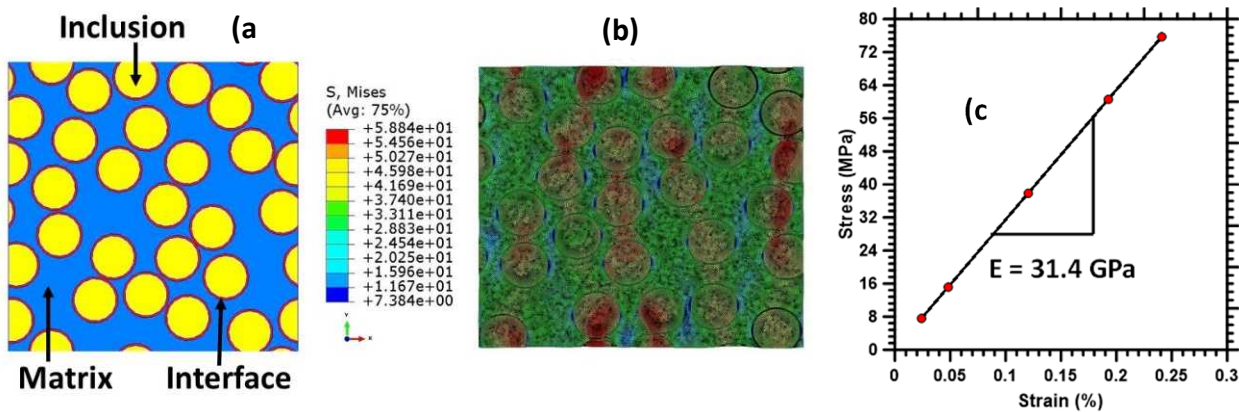


Figure 2: (a) 2D FE model showing the inclusions, matrix, and the interface, (b) microstructural stress distribution, and (c) linear constitutive relationship for mortar with quartz inclusion

### 3. PREDICTION OF CRACK PROPAGATION AND FRACTURE RESPONSE OF MORTARS

Two different methods, i.e., XFEM and peridynamics are used to predict crack propagation and fracture properties of mortars. Brief discussions of theoretical formulations associated with these methods are provided in the respective sub-sections. The predicted values from the simulation schemes are verified against values obtained experimentally using closed-loop crack mouth opening displacement (CMOD)-controlled testing (CMOD acting as the feedback signal) of notched mortar beams under three-point-bending. For experimental evaluation of fracture behavior, four replicate beams were tested. The notch depth was 19 mm (corresponding to a notch depth-to-beam depth ratio of 0.25). The beams were tested in a CMOD-controlled mode during the loading cycles and in a load-controlled mode during the unloading cycles.

#### 3.1 Simulation using Extended Finite Element Method (XFEM)

##### 3.1.1 XFEM Formulation for Damage Prediction in Mortars/Concrete

XFEM has been used extensively in modeling the fracture behavior of different classes of materials (Bayesteh and Mohammadi 2013; Curiel Sosa and Karapurath 2012; Eftekhari et al. 2014; Feerick et al. 2013; Ye et al. 2012). In the XFEM framework, the displacement field consists of two parts – one continuous and the other discontinuous. The former is the standard displacement field corresponding to an uncracked situation. Local enrichment functions are incorporated in the FE approximation in order to model the crack (discontinuities) in an efficient manner. The enriched functions have additional degrees of freedom and simulate path-independent crack initiation and propagation based on the damage criteria provided. The approximation of displacement vector function with the partition of unity enrichment is given as (Belytschko and Black 1999; Motamed et al. 2013):

$$u = \sum_{I=1}^N N_I(x)[u_I + H(x)a_I + \sum_{\alpha=1}^4 F_{\alpha}(x)b_I^{\alpha}] \quad (8)$$

where,  $N_I(x)$  are the conventional nodal shape functions at node  $I$ ,  $u_I$  is the nodal displacement vector associated with the continuous part of the finite element solution;  $a_I$  is the nodal enriched degree of freedom vector,  $H(x)$  is the Heaviside function;  $b_I^{\alpha}$  is the product of nodal enriched degree of freedom vector, and  $F_{\alpha}(x)$  are the associated elastic asymptotic crack-tip functions.  $H(x)$  is given as:

$$H(x) = 1 \text{ if } (x - x^*) \cdot n \geq 0 \quad (9)$$

If Equation 9 is not satisfied, it is equal to -1. Here,  $x$  is a sample Gauss point,  $x^*$  is the point on the crack closest to  $x$ , and  $n$  is the unit outward normal to the crack at  $x^*$ . The asymptotic crack tip functions  $F_\alpha$  are given as (Belytschko and Black 1999):

$$F_\alpha(x) = [\sqrt{r} \sin \frac{\theta}{2}, \sqrt{r} \cos \frac{\theta}{2}, \sqrt{r} \sin \theta \cdot \sin \frac{\theta}{2}, \sqrt{r} \sin \theta \cdot \cos \frac{\theta}{2}] \quad (10)$$

where the crack tip is at the origin of the polar coordinate system and  $\theta=0$  is the tangent to the crack tip. The XFEM damage model requires appropriate damage initiation criteria. The maximum principal stress criteria is adopted in this study and the crack is considered to be initiated if the maximum principal stress exceeds the tensile strength of the mortar. A bilinear traction-separation law (Bažant 2002; Roesler *et al.* 2007) is used for damage propagation, as shown in Equations 11a and 11b. The fracture energy ( $G_F$ ) is the area under the entire traction-separation curve, given as:

$$G_F = \int_0^\infty f(w) dw \quad (11a)$$

$$f(w) = \begin{cases} f_t - (f_t - f_1) \frac{w}{w_1} & \text{for } w \leq w_1 \\ f_1 - f_1 \frac{(w-w_1)}{(w_c-w_1)} & \text{for } w_1 > w \end{cases} \quad (11b)$$

where  $f_t$  is the tensile strength of the material,  $w_c$  is the critical crack tip opening displacement, and  $f_1$  and  $w_1$  are the stress and opening displacement corresponding to the kink in the bilinear traction-separation curve.

The numerical simulation framework incorporates the Concrete Damage-Plasticity (CDP) model (Jankowiak and Lodygowski 2005; Voyatzis *et al.* 2008) beyond the linear elastic regime for fracture simulation. CDP is a material model based on a combination of damage and plasticity theory. The plasticity theory is used to describe both the compressive and tensile response of concrete, while the damage theory is used for the cyclic and unloading characteristics. In this model, isotropic damage is represented as:

$$\sigma = (1 - d) D_0^{el} : (\varepsilon - \varepsilon^{pl}) = D^{el} : (\varepsilon - \varepsilon^{pl}) \quad (12)$$

where  $\sigma$  is the Cauchy stress tensor,  $d$  is the scalar stiffness degradation variable,  $\varepsilon$  is the strain tensor,  $\varepsilon^{pl}$  is the plastic strain,  $D_0^{el}$  is the initial elastic stiffness of the material, and  $D^{el}$  is the degraded elastic stiffness tensor. The effective stress tensor  $\bar{\sigma}$  is given as:

$$\bar{\sigma} = D_0^{el} : (\varepsilon - \varepsilon^{pl}) \quad (13)$$

Damage states in tension and compression are characterized independently by two hardening variables which are the equivalent plastic strains in compression and tension respectively. The plastic flow is given as (Jankowiak and Lodygowski 2005):

$$\dot{\varepsilon}^{pl} = \dot{\lambda} \frac{\partial G(\bar{\sigma})}{d\bar{\sigma}} \quad (14)$$

where, the flow potential, G is given using a Drucker-Prager hyperbolic function as:

$$G = \sqrt{(f_c - m \cdot f_t \cdot \tan \beta)^2 + \bar{q}^2} - \bar{p} \cdot \tan \beta - \sigma \quad (15)$$

Here,  $f_t$  is the tensile strength and  $f_c$  is the compressive strength,  $\beta$  is the dilation angle and  $m$  is the eccentricity of the plastic potential surface,  $\bar{p}$  is the effective hydrostatic stress and  $\bar{q}$  is the Mises equivalent effective stress. The CDP model uses a yield condition based on loading function:

$$F = \frac{1}{1 - \alpha} (\bar{q} - 3 \cdot \alpha \cdot \bar{p} + \theta(\varepsilon^{pl}) \langle \bar{\sigma}_{max} \rangle - \gamma \langle -\bar{\sigma}_{max} \rangle) - \bar{\sigma}_c(\varepsilon^{pl}) \quad (16)$$

where the function  $\theta(\varepsilon^{pl})$  is given as:

$$\theta(\varepsilon^{pl}) = \frac{\bar{\sigma}_c(\varepsilon_c^{pl})}{\bar{\sigma}_t(\varepsilon_t^{pl})} (1 - \alpha) - (1 + \alpha) \quad (17)$$

The parameter  $\alpha$ , which is based on the ratio of biaxial compressive strength ( $f_{b0}$ ) to uniaxial compressive strength ( $f_c$ ), is defined as:

$$\alpha = \frac{(f_{b0}/f_c) - 1}{2(f_{b0}/f_c) - 1} \quad (18)$$

### 3.1.2 Numerical Simulation of Three Point Bending Test for Mortar Beams using XFEM in ABAQUS

A 2D XFEM model is used to simulate three-point bending of a notched mortar beam. The beam has a span of 100 mm, and a cross section of 25 mm x 25 mm. Experimental details were mentioned earlier in this paper. The meshed beam model is shown in Figure 3.

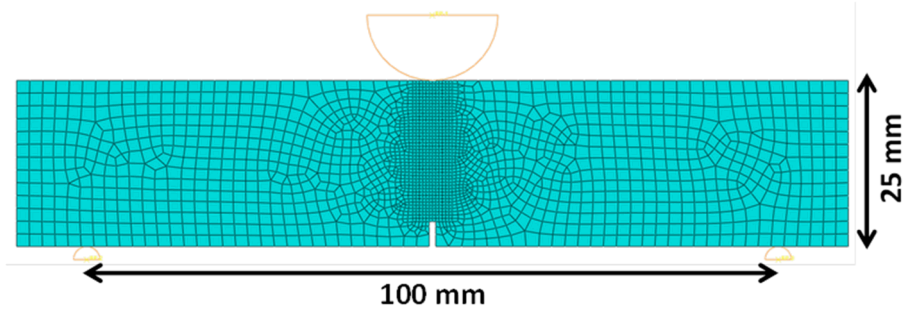


Figure 3: Meshed notched beam for 2D XFEM simulation

The beam has an initial notch, which is 1 mm wide and 3.75 mm deep, at the mid-span. The two pin supports and the loading head at the top are defined as rigid bodies. The displacement is applied at a reference point tied to the loading head. Traction-separation behavior is quantified using data on the cement mortar made using the same materials and proportions, reported in an earlier publication (Das et al. 2015a). The values for the concrete damage plasticity (CDP) variables, i.e.,  $\beta$  which is the dilation angle at high confining pressure,  $m$  which is the eccentricity of the plastic potential surface,  $\gamma$  which is the parameter that determines the shape of the loading surface in the deviatoric plane, and  $s$ , the ratio of biaxial compressive strength to uniaxial compressive strength of concrete, are adopted from (Jankowiak and Lodygowski 2005). While these parameters are provided for concrete in (Jankowiak and Lodygowski 2005), they are used in this study for mortars also, for lack of better experimental data on these parameters. The material parameters for XFEM simulation are shown in Table 2 (Das et al. 2015a; Kim and Abu Al-Rub 2011 p.; Yang 1998).

Table 2: Properties of the mortar and parameters for XFEM simulation

| E(GPa) | $\nu$ | Max. principal stress (MPa) | $G_F$ (N/mm) | CDP model parameters |     |          |      |
|--------|-------|-----------------------------|--------------|----------------------|-----|----------|------|
|        |       |                             |              | $\beta$              | $m$ | $\gamma$ | $f$  |
| 31.4   | 0.22  | 3.0                         | 0.035        | 38°                  | 1.0 | 0.67     | 1.12 |

The uniaxial tension and compression behavior of cement mortar for CDP model, adopted from (Kim and Abu Al-Rub 2011), are shown in Figure 4. Figure 5 shows the generated load-crack mouth opening displacement (CMOD) response obtained from the XFEM simulation.

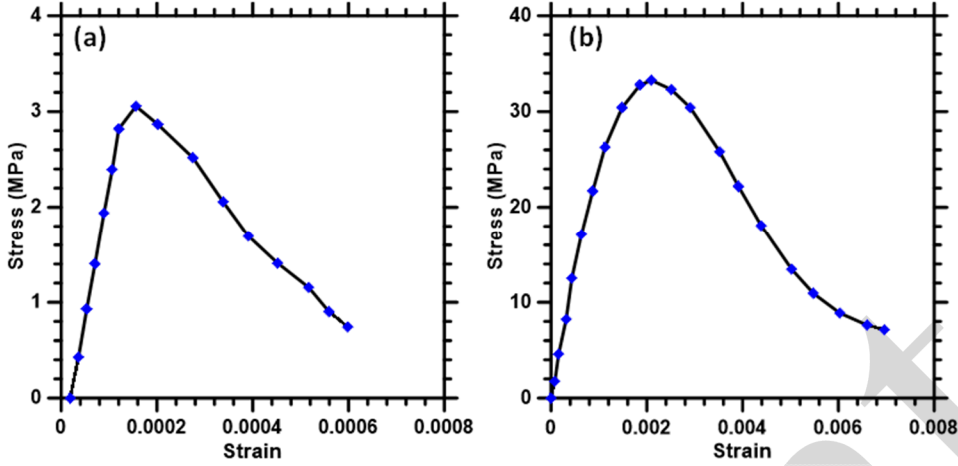


Figure 4: Representative: (a) uniaxial tension, and (b) uniaxial compression behavior implemented in the concrete damage plasticity (CDP) model. Data from (Jankowiak and Lodygowski 2005).

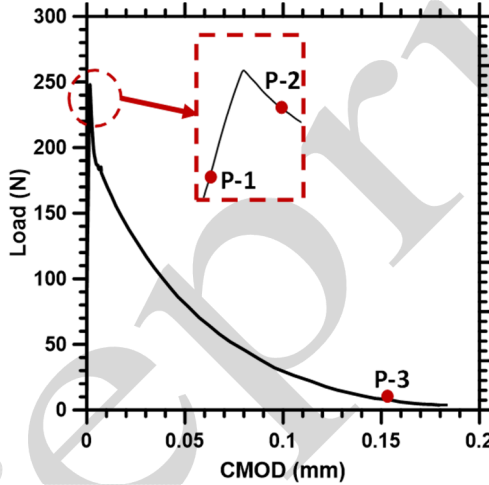


Figure 5: Simulated Load-CMOD response of the mortar beam using XFEM

The maximum principal stress contours at three different stages in the load-CMOD response obtained through the implementation of the CDP model in the XFEM framework are shown in Figure 6. Point P-1 in Figure 6 corresponds to 85% of the peak load in the pre-peak regime whereas point P-2 corresponds to 95% of the peak load in the post-peak regime. Point P-3 is chosen at a CMOD value of 0.16 mm, which corresponds to a CMOD very close to ultimate failure. Figure 6(a) does not show the formation of a crack since the maximum principal stress (2.62 MPa) is smaller than the considered tensile strength (3 MPa) of cement mortar. The crack is observed to initiate close to the peak load when the maximum principal stress equals the tensile strength. Figure 6(b) shows the stress contour corresponding to 95% of the peak load in the post peak regime. The crack has begun to propagate at this stage and is roughly at the mid-height of the specimen at this load level. The stress concentration near the tip of the crack is also visible as expected. Figure 6(c) shows almost complete propagation of the crack near failure.

Crack extension-related values at 95% of the peak load in the post-peak regime can be used to calculate the Mode I stress intensity fracture (fracture toughness),  $K_{IC}$ , of the cement mortar using the two-parameter fracture model (TPFM) as follows (Gdoutos 2006; Nunes and Reis 2012):

$$K_{IC} = \frac{PL}{bd^{3/2}} F\left[\frac{a_{eff}}{d}\right] \quad (19a)$$

$$F\left[\frac{a_{eff}}{d}\right] = [2.9\left(\frac{a_{eff}}{d}\right)^{1/2} - 4.6\left(\frac{a_{eff}}{d}\right)^{3/2} + 21.8\left(\frac{a_{eff}}{d}\right)^{5/2} - 37.6\left(\frac{a_{eff}}{d}\right)^{7/2} + 38.7\left(\frac{a_{eff}}{d}\right)^{9/2}] \quad (19b)$$

where the effective crack length,  $a_{eff} = a_0 + \Delta a$ . The critical crack tip opening displacement (CTOD<sub>C</sub>), which is another fracture parameter in the TPFM is computed as the CTOD value at 95% of the peak load in the post-peak regime (P-2 in Figure 5). The values of  $K_{IC}$  and CTOD<sub>C</sub> are 27.4 MPa.mm<sup>0.5</sup> and 0.012 mm respectively. There is a very good correlation between the  $K_{IC}$  and CTOD<sub>C</sub> values obtained from the XFEM simulation and the experimental measurements [41] (26.4 MPa.mm<sup>0.5</sup> and 0.0125 mm from experimental load-CMOD data, by employing TPFM).

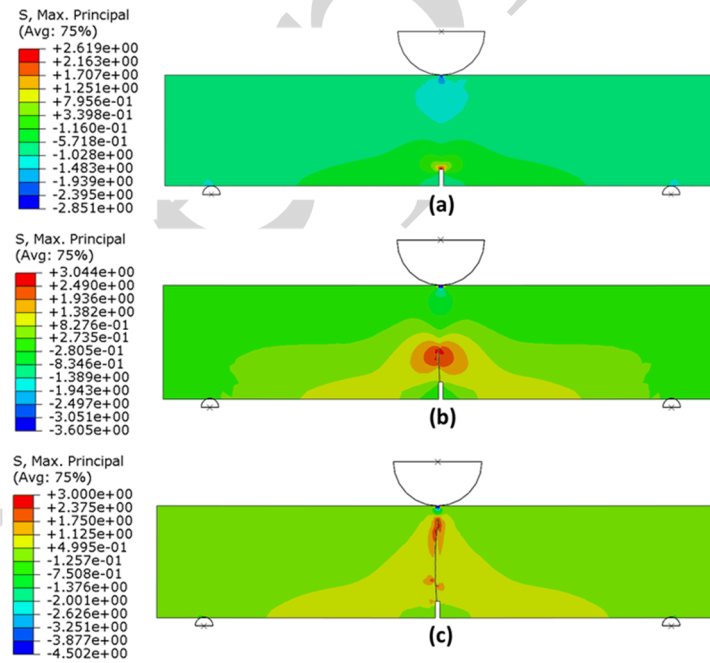


Figure 6: Maximum principal stress contours: (a) P-1 (85% of the peak load in pre-peak regime); (b) P-2 (95% of the peak load in post-peak regime) and (c) P-3 (near failure: CMOD of 0.16 mm)

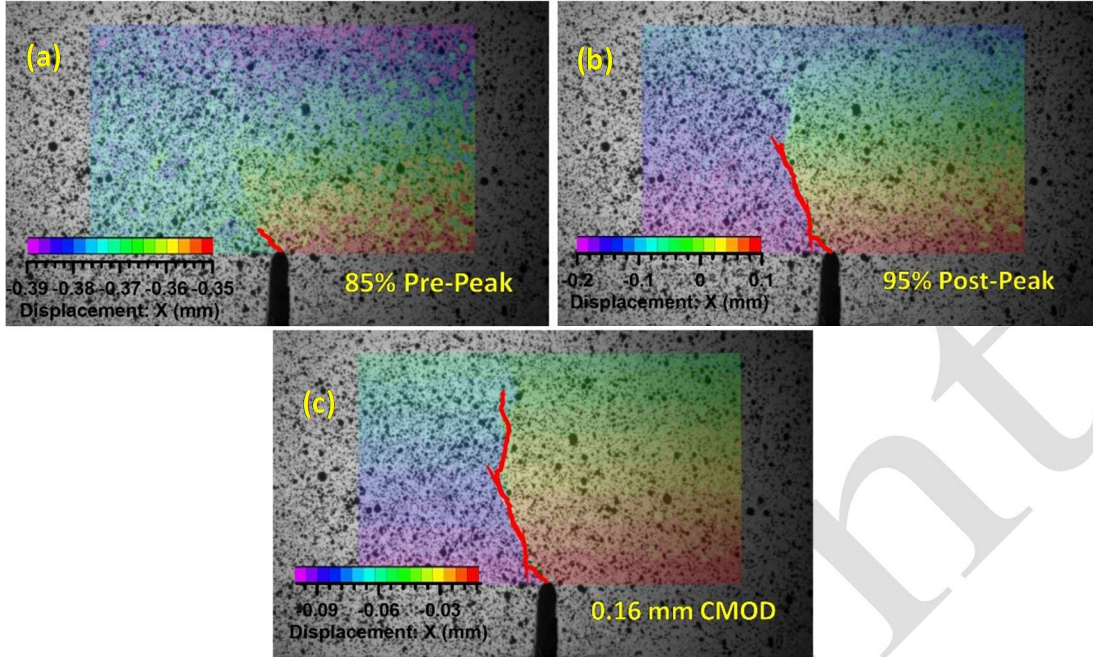


Figure 7: Images processed using digital image correlation (DIC), with the crack corresponding to the three locations P-1 to P-3 in the load-CMOD plot: (a) 85% of the peak load in pre-peak regime, (b) 95% of the peak load in post-peak regime, and (c) near failure: CMOD of 0.16 mm.

Digital image correlation (DIC), which is a non-contact optical method that can be used to analyze digital images to extract the full displacement field on a specimen's surface (Chu et al. 1985; Pan et al. 2009), was used along with the experimental determination of fracture parameters. The time series information from the data acquisition system connected to the loading frame was matched with that from the photographs of the analysis region (images were taken by a CCD camera every 5 seconds) and image correlation was carried out. Figure 7 shows the 2D horizontal displacement fields for the mortar beam corresponding to points P-1 to P-3 in Figure 5. The jump in the horizontal displacement above the notch indicates crack initiation and propagation (Das et al. 2014a). The displacement jump and the visible crack in the images are well correlated, indicated by the dark lines in the images shown in Figures 7(a)-(c). CTOD and crack extension can also be directly measured using DIC (Das et al. 2014a), from which the determined  $K_{IC}$  and  $CTOD_C$  values were  $30.1 \text{ MPa} \cdot \text{mm}^{0.5}$  and  $0.017 \text{ mm}$  respectively, which agrees well with those determined using the TPFM method and XFEM simulations. Moreover, a comparison of Figures 6 and 7 shows that the crack paths as a function of load are also captured adequately by the XFEM simulations. Importantly, the application of CDP parameters to mortar does not seem to inhibit the predictive capacity of XFEM simulations.

### 3.2 Simulation using Peridynamics

#### 3.2.1 Peridynamic Theory

The peridynamic theory was developed by Silling (Silling and Askari 2005; Silling and Bobaru 2005) to include damage and fracture into the formulation without the use of special mathematical techniques to account for points at which discontinuities occur. It is envisaged as a theory to unify the mathematical and computational modeling of continuous media, crack growth, and discrete particles (Silling and Cox 2014). In peridynamics, every material point interacts directly with other points within a distance of  $\delta$ , called the horizon, through peridynamic bonds. This is schematically shown in Figure 8(a). The horizon represents the maximum interaction distance for material points, and is generally an effective material length scale. The vector from  $x$  to any point in its family  $\mathcal{H}(x)$  in the reference configuration is called a bond. Figure 8(b) shows the bond forces that allows for discontinuity. The micro-elastic moduli of each bond are different, denoted by  $c_x$ . The horizon, though shown as a circle here, can have any arbitrary shape as long as the micro-modulus function satisfies the linear and angular momentum criteria (Hu 2012).

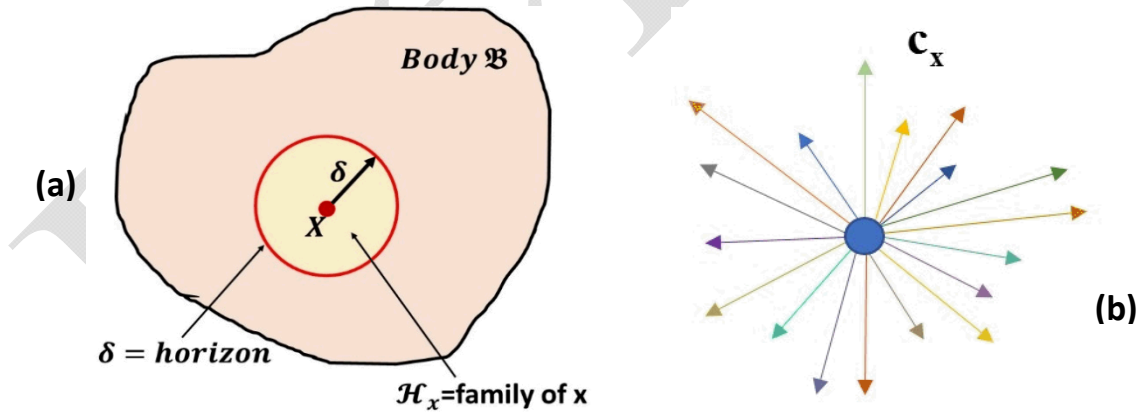


Figure 8: (a) Horizon and family, and (b) bond forces in peridynamics

The equation of motion represented in the bond-based theory of peridynamics defines the acceleration of any particle at  $x$  in the reference configuration at time  $t$  as (Silling and Lehoucq 2010):

$$\rho(\mathbf{x})\ddot{\mathbf{u}}(\mathbf{x}, t) = \int_{\mathcal{H}_x} \mathbf{f}(\mathbf{u}(\mathbf{x}', t) - \mathbf{u}(\mathbf{x}, t), \mathbf{x}' - \mathbf{x}) dV_{\mathbf{x}'} + \mathbf{b}(\mathbf{x}, t) \quad (20)$$

where  $\mathcal{H}_x$  is a neighborhood of  $\mathbf{x}$  in a body  $\mathcal{B}$ ,  $\mathbf{u}$  is the displacement vector field,  $\mathbf{b}$  is a prescribed body force density field,  $\rho$  is mass density field in the reference configuration, and the function  $\mathbf{f}$  is a pairwise bond force density field whose value is the force vector (per unit square of the volume) that the particle  $\mathbf{x}'$  exerts on the particle  $\mathbf{x}$  (Silling and Askari 2005).

The relative position of two particles ( $\xi$ ) and the relative displacement vector at their end points ( $\eta$ ) are represented as:

$$\xi = \mathbf{x}' - \mathbf{x} \quad (21)$$

$$\eta = \mathbf{u}(\mathbf{x}', t) - \mathbf{u}(\mathbf{x}, t) \quad (22)$$

where  $\eta + \xi$  represents the current relative position vector between the particles. If the bond responses are considered to be independent of others, as is the case in bond-based peridynamics, the resulting material model is a relationship between the bond force density and the bond strain. Assuming the bond-based material to be linearly elastic, the bond force density field and the bond strain are related as:

$$f = c(\xi)s\mathbf{M} \quad (23)$$

In the above equation,  $s$  is the bond strain and  $\mathbf{M}$  is the deformed bond direction unit vector.

Damage is implemented in bond-based peridynamic models using bond breakage. At a certain critical bond stretch,  $\varepsilon_c$ , the bond is considered to fail irreversibly. The progression of cracking is determined by the field equations and the constitutive model at the bond level. In other words, the idea of stress intensity factor is not used in peridynamics.

The bond-based peridynamic theory, which is a continuum extension of molecular dynamics, is limited because of the fact that the response of a material at a point is determined by the deformation of each individual bond independently. The Poisson's ratio is always 0.25 in this case (Ren et al. 2017). To overcome this limitation, a more general peridynamic framework was developed, where each bond force depends on the collective deformation of all the bonds within the horizon (Silling and Lehoucq 2010). This is the basis of state-based peridynamics because the mathematical objects that convey information about the collective deformation of bonds are called peridynamic states (Silling et al. 2007). This approach allows the response of a material at a point to depend on the deformation of all

bonds connected to the point. The bond-based theory then becomes a special case of the state-based theory.

Peridynamics is currently being implemented in commercially available FE analysis software. However, the current capabilities of these FEA suites are limited in scope. In this study, a beta version of peridynamics as implemented in LS-DYNA is used. This version includes only brittle failure analysis based on a Galerkin finite element method with the bond-based peridynamics model. The discontinuous Galerkin approach is used within the context of classical peridynamics equations. As the examples in this section will show, this makes it possible to use traditional finite element approach including using the finite element mesh to construct the peridynamics numerical solution (Ren et al. 2017). This approach alleviates to some degree, the issue of non-uniform discretization and difficulties in prescribing boundary conditions and kinematic constraints that plague conventional applications of bond-based and state-based peridynamics. The implementation utilizes the prototype microelastic brittle (PMB) material model, which is a linear isotropic material model where each bond is treated as a linear spring, resulting in an implied Poisson's ratio of 0.25. With this, the micro-elastic modulus,  $c_x$ , of each bond, is calculated using linear equations with respect to the classic elastic modulus,  $E$ , as:

$$3E = \sum_{\xi} \frac{1}{2} c_x |\xi| \Delta V_{x'} \quad (24)$$

where  $\Delta V_{x'}$  is the change in volume of the surrounding point,  $\mathbf{X}'$ , and  $\xi$  is the relative position between point  $\mathbf{X}$  and its neighbor  $\mathbf{X}'$ , similar to Equation 21. However, the formulation of the peridynamic model in LS-DYNA defines the relative positions and displacements using Gaussian points and shape functions, written as:

$$\xi(X^g) = N^A(X^g)X^A - N^{A'}(X^{g'})X^{A'} \quad (25)$$

$$\eta(X^g) = N^A(X^g)u^A - N^{A'}(X^{g'})u^{A'} \quad (26)$$

where  $N^A(X^g)$  and  $N^{A'}(X^{g'})$  are the shape functions of a Gaussian point  $\mathbf{X}^g$  and its neighbor Gaussian point  $\mathbf{X}^{g'}$  within the horizon, respectively. Then a bond,  $\xi$ , and the bond deformation,  $\eta$ , are used in the Galerkin weak form as [18]:

$$\int_{\Omega} \rho \ddot{u}_i^A N^A(\mathbf{X}) N^B(\mathbf{X}) dV_{\mathbf{X}} = \int_{\Omega} \left( \int_{H_X} f_i(\boldsymbol{\eta}, \xi) dV_{\mathbf{X}'} \right) N^B(\mathbf{X}) dV_{\mathbf{X}} + \int_{\Omega} b_i(\mathbf{X}) N^B(\mathbf{X}) dV_{\mathbf{X}} \quad (27)$$

where  $u_i^A$  denotes the nodal displacement  $u_i$  of node A, and  $\Omega$  is the computational domain of the peridynamics problem described. With this weak form, the computational domain is partitioned by a FEM mesh, and not by particles as is done in a typical mesh free type of peridynamic implementation.

The critical bond stretch,  $s_c$ , of each bond in the LS-DYNA implementation is calculated based on the idea that all bonds crossing a crack surface must be broken to completely form the crack surface, resulting in (Ren et al. 2017):

$$s_c = \sqrt{\frac{10G_c}{\pi c \delta^5}} \quad (28)$$

where  $G_c$  is the fracture energy release rate. The critical bond stretch in Equation 28 is not a constant value for all bonds, as the microelastic modulus,  $c$ , calculated from Equation 24 depends on the level and nature of mesh discretization as well as the location. This results in a non-standard conversion of the fracture energy release rate to critical bond stretch, which is mesh dependent. Therefore, the value defined for the fracture energy release rate may not produce the expected results, as will be discussed later in this paper.

### 3.2.2 Numerical Simulation of Three-point-bending Test of Mortar Beams using Peridynamics

The 3D mortar beam with the peridynamic material model for use in LS-DYNA is shown in Figure 9 (note that, for XFEM, a 2D simulation was used).

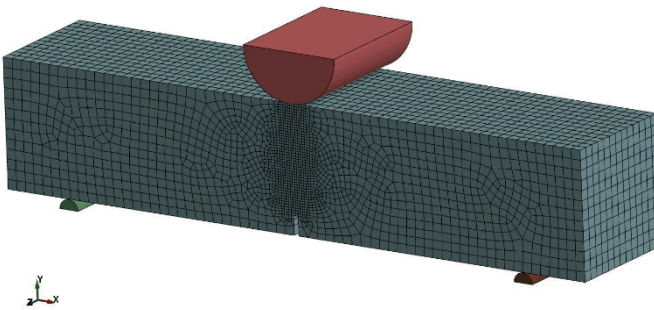


Figure 9: Meshed notched beam for peridynamics simulations

The necessary material input parameters are the mass density, elastic modulus (from the microstructure guided numerical method reported earlier) and fracture energy release rate as summarized in Table 3.

Table 3: Summary of input parameters for LS-DYNA peridynamic model

|                              |           |
|------------------------------|-----------|
| $\rho$ (kN/mm <sup>3</sup> ) | $20*10^9$ |
| E (MPa)                      | 31400     |
| $G_c$ (N/mm)                 | 0.035     |
| DR <sup>1</sup> (--)         | 0.81      |

It is seen that the peridynamic method can simulate fracture using a fewer number of parameters, which is advantageous. However, since the value of the critical bond strength (Equation 28), is not readily available, a calibration process was required. Note that the critical bond stretch (at which the bond fails, and cracking happens) is dependent on the horizon  $\delta$ , micro-elastic modulus  $c$ , and the fracture energy release rate (Equation 28). In the PMB model, when the scale of modeling represents the material as a homogeneous continuum, as is the case here, the horizon is chosen as a matter of convenience (Silling and Cox 2014). In practice, for situations where a material length scale is not directly evident, the size of the horizon is sequentially reduced until convergence is obtained [64]. LS-DYNA uses a parameter termed DR, which is the ratio of the horizon radius and a characteristic length  $l_e$  (which is the diagonal length of the each element [18]). A DR value of 0.81 facilitated convergence in this study, and was used to determine the horizon size. The changes in horizon radius results in considerable changes in the critical bond stretch values, and thus the predicted fracture parameters. In this work, a calibration exercise was performed in which all other parameters were kept the same, while the value of fracture energy was varied to match the simulated peak load with the experimental data. The input fracture energy release rate obtained from this exercise was 0.035 N/mm, which is in line with the strain energy release rates determined experimentally for mortars (Das et al. 2014a). Figure 10 shows the stress states in the beam from peridynamic simulations corresponding to different load states, similar to those obtained from XFEM simulations (Figure 6). The load-CMOD response is shown in Figure 11.

While the critical stress intensity factor ( $K_{IC}$ ) from the peridynamic simulation matched that from the experiment and XFEM simulation, the CMOD (computed at 95% of the peak load in the post-peak regime) was about half of the expected value. This may be attributed, in addition to the other limitations stated earlier, to the type of FE simulation carried out in the LS-DYNA PMB material model framework. An explicit finite element simulation (which is the currently available method in LS-DYNA)

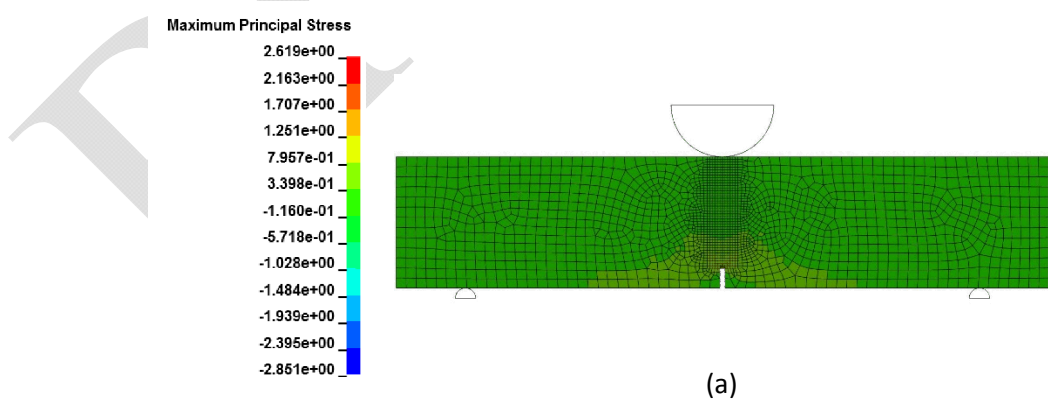
---

<sup>1</sup> DR is an LS-DYNA parameter with a recommended value between 0.6 and 1.2, which is used to determine the size of the horizon based on the characteristic length of the element.

was carried out instead of an implicit analysis and it is likely that, as the crack tip propagates near the boundary, the stress waves between the crack tip and boundary affects the displacement computations. The maximum principal stress contours in the peridynamic simulation, Figure 10, also match well with the XFEM simulation results shown in Figure 6 and the experimental DIC crack profiles shown in Figure 7. The final comparison of the numerically obtained values with experimental results is shown in Table 3.

Table 3: Comparison of the  $K_{IC}$  and  $CTOD_c$  values determined using XFEM, Peridynamics and experiments (both TPFM and DIC)

| Fracture toughness, $K_{IC}$ (MPa.mm $^{0.5}$ ) |      |                    |                   | Critical crack tip opening displacement, $CTOD_c$ (mm) |       |                    |                   |
|---|------|--------------------|-------------------|--|-------|--------------------|-------------------|
| XFEM  | PD   | Experiments (TPFM) | Experiments (DIC) | XFEM   | PD    | Experiments (TPFM) | Experiments (DIC) |
| 27.4  | 28.6 | 26.4               | 30.1              | 0.012  | 0.006 | 0.0125             | 0.017             |



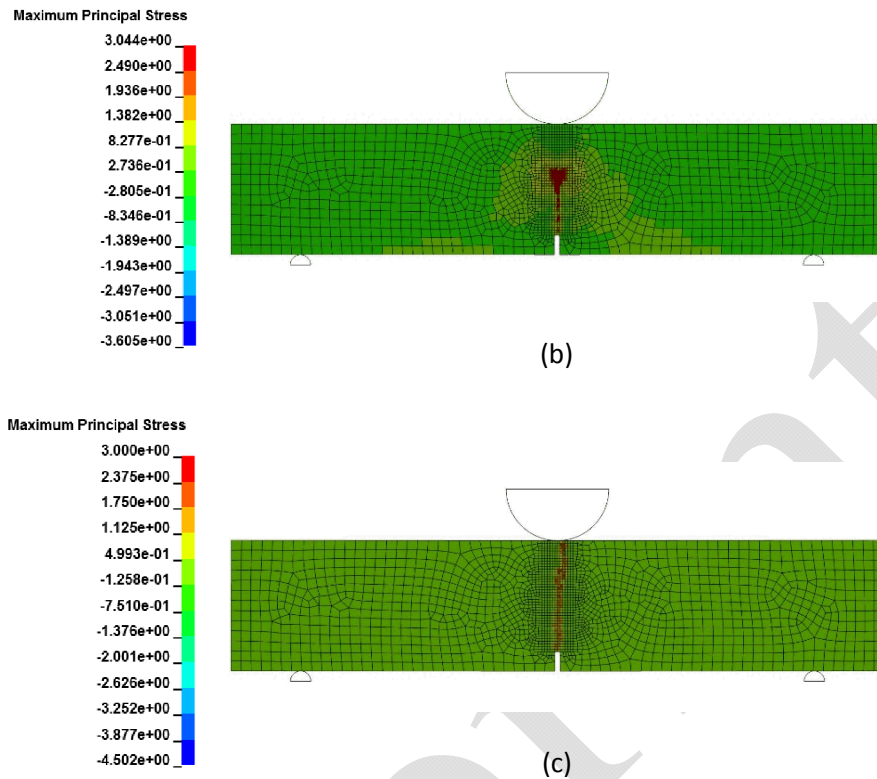


Figure 10: Maximum principal stress contours for peridynamic simulation: (a) P-1 (85% of the peak load in pre-peak regime); (b) P-2 (95% of the peak load in post-peak regime) and (c) P-3 (near failure: CMOD: 0.06 mm)

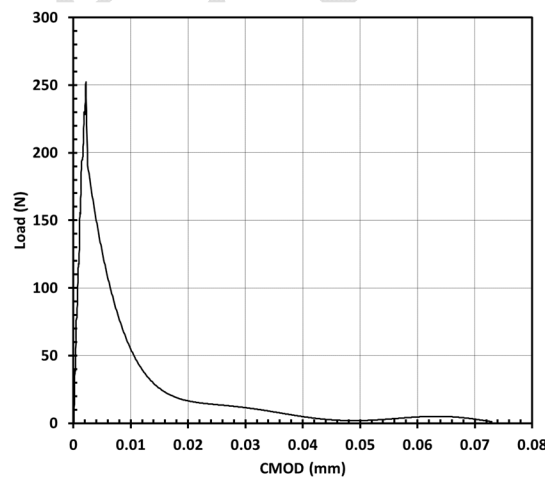


Figure 11: Load-CMOD response obtained from peridynamic simulations

#### **4. SUMMARY AND CONCLUSIONS**

The fracture response of notched cementitious mortar beams under three-point bending were simulated using two advantageous modeling and simulation frameworks – XFEM and peridynamics. The input elastic response of the mortar required for fracture modeling was obtained through a microstructure-guided constitutive modeling scheme using conventional finite element analysis.

A 2D model was used for XFEM-based fracture modeling. The total fracture energy obtained from a bilinear traction-separation response was used in conjunction with the concrete damage plasticity (CDP) model in ABAQUS to simulate fracture. Due to lack of reported CDP parameters for mortars, the corresponding published parameters for concrete were used in this study. The maximum principal stress criteria was adopted in this study for damage initiation. The fracture parameters ( $K_{IC}$  and  $CTOD_C$ ) extracted from the XFEM-predicted load-CMOD response were found to be in very good agreement with those predicted by employing the two-parameter fracture model (TPFM) to the experimental load-CMOD response of the mortar. The fracture simulations were found to be not very sensitive to the CDP parameters.

The bond-based peridynamic simulation of fracture was implemented in a 3D model in LS-DYNA. A prototype microelastic brittle (PMB) material model was used, which restricts the Poisson's ratio to a constant value of 0.25. The peridynamic method was able to simulate fracture using a fewer number of parameters; however a calibration process was required since the critical bond strength could not be obtained. The calibration was based on adjusting the fracture energy release rate so as to match the peak load from experiments. The choice of the horizon value in the PMB model was also dictated by convergence necessities, which influenced the fracture parameters. Despite these approximations,  $K_{IC}$  and crack extension were reasonably well-predicted by the peridynamics model. Both XFEM and peridynamics adequately predicted the crack extension at different loading and unloading stages, which were experimentally determined using DIC.

#### **5. ACKNOWLEDGEMENTS**

The authors gratefully acknowledge financial support for this research provided by the U.S. Department of Energy, Nuclear Engineering University Program (NEUP) under grant no. DE-NE0008398. SD acknowledges the support from College of Engineering (COE) and Department of Civil and Environmental Engineering at the University of Rhode Island (URI). The contents of this paper reflect the views of the authors who are responsible for the facts and accuracy of the data presented herein, and

do not necessarily reflect the views and policies of the funding agency, nor do the contents constitute a standard, specification, or a regulation.

## 6. REFERENCES

- Akkurt, I., Basyigit, C., Kilincarslan, S., Mavi, B., and Akkurt, A. (2006). "Radiation shielding of concretes containing different aggregates." *Cement and Concrete Composites*, 28(2), 153–157.
- Al-Jabri, K. S., Hago, A. W., Al-Nuaimi, A. S., and Al-Saidy, A. H. (2005). "Concrete blocks for thermal insulation in hot climate." *Cement and Concrete Research*, 35(8), 1472–1479.
- Bayesteh, H., and Mohammadi, S. (2013). "XFEM fracture analysis of orthotropic functionally graded materials." *Composites Part B: Engineering*, 44(1), 8–25.
- Bažant, Z. P. (2002). "Concrete fracture models: testing and practice." *Engineering Fracture Mechanics*, 69(2), 165–205.
- Belytschko, T., and Black, T. (1999). "Elastic crack growth in finite elements with minimal remeshing." *International journal for numerical methods in engineering*, 45(5), 601–620.
- Bobiński, J., and Tejchman, J. (2016). "A coupled constitutive model for fracture in plain concrete based on continuum theory with non-local softening and eXtended Finite Element Method." *Finite Elements in Analysis and Design*, 114, 1–21.
- Bolander, J. E., and Sukumar, N. (2005). "Irregular lattice model for quasistatic crack propagation." *Physical Review B*, 71(9), 094106.
- Chu, T. C., Ranson, W. F., and Sutton, M. A. (1985). "Applications of digital-image-correlation techniques to experimental mechanics." *Experimental Mechanics*, 25(3), 232–244.
- Curiel Sosa, J. L., and Karapurath, N. (2012). "Delamination modelling of GLARE using the extended finite element method." *Composites Science and Technology*, 72(7), 788–791.
- Cusson, D., and Hoogeveen, T. (2008). "Internal curing of high-performance concrete with pre-soaked fine lightweight aggregate for prevention of autogenous shrinkage cracking." *Cement and Concrete Research*, 38(6), 757–765.
- Das, S., Aguayo, M., Dey, V., Kachala, R., Mobasher, B., Sant, G., and Neithalath, N. (2014a). "The fracture response of blended formulations containing limestone powder: Evaluations using two-parameter fracture model and digital image correlation." *Cement and Concrete Composites*, 53, 316–326.
- Das, S., Aguayo, M., Sant, G., Mobasher, B., and Neithalath, N. (2015a). "Fracture process zone and tensile behavior of blended binders containing limestone powder." *Cement and Concrete Research*, 73, 51–62.
- Das, S., Maroli, A., and Neithalath, N. (2016a). "Finite element-based micromechanical modeling of the influence of phase properties on the elastic response of cementitious mortars." *Construction and Building Materials*, 127, 153–166.
- Das, S., Maroli, A., Singh, S. S., Stannard, T., Xiao, X., Chawla, N., and Neithalath, N. (2016b). "A microstructure-guided constitutive modeling approach for random heterogeneous materials: Application to structural binders." *Computational Materials Science*, 119, 52–64.
- Das, S., Souliman, B., Stone, D., and Neithalath, N. (2014b). "Synthesis and Properties of a Novel Structural Binder Utilizing the Chemistry of Iron Carbonation." *ACS Applied Materials & Interfaces*, 6(11), 8295–8304.
- Das, S., Yang, P., Singh, S. S., Mertens, J. C. E., Xiao, X., Chawla, N., and Neithalath, N. (2015b). "Effective properties of a fly ash geopolymers: Synergistic application of X-ray

- synchrotron tomography, nanoindentation, and homogenization models.” *Cement and Concrete Research*, 2015(2015).
- Eftekhari, M., Hatefi Ardakani, S., and Mohammadi, S. (2014). “An XFEM multiscale approach for fracture analysis of carbon nanotube reinforced concrete.” *Theoretical and Applied Fracture Mechanics*, Multiscale Modeling of Material Failure, 72, 64–75.
- Feerick, E. M., Liu, X. (Cheryl), and McGarry, P. (2013). “Anisotropic mode-dependent damage of cortical bone using the extended finite element method (XFEM).” *Journal of the Mechanical Behavior of Biomedical Materials*, 20, 77–89.
- Fernandes, F., Manari, S., Aguayo, M., Santos, K., Oey, T., Wei, Z., Falzone, G., Neithalath, N., and Sant, G. (2014). “On the feasibility of using phase change materials (PCMs) to mitigate thermal cracking in cementitious materials.” *Cement and Concrete Composites*, 51, 14–26.
- Gdoutos, E. E. (2006). *Fracture mechanics: an introduction*. Springer.
- Golewski, G. L., Golewski, P., and Sadowski, T. (2012). “Numerical modelling crack propagation under Mode II fracture in plain concretes containing siliceous fly-ash additive using XFEM method.” *Computational Materials Science*, 62, 75–78.
- Grondin, F., and Matallah, M. (2014). “How to consider the Interfacial Transition Zones in the finite element modelling of concrete?” *Cement and Concrete Research*, 58, 67–75.
- Hashin, Z., and Monteiro, P. J. M. (2002). “An inverse method to determine the elastic properties of the interphase between the aggregate and the cement paste.” *Cement and Concrete Research*, 32(8), 1291–1300.
- Hembade, L., Neithalath, N., and Rajan, S. D. (2013). “Understanding the energy implications of phase-change materials in concrete walls through finite-element analysis.” *Journal of Energy Engineering*, 140(1), 04013009.
- Hernández-Olivares, F., Barluenga, G., Bollati, M., and Witoszek, B. (2002). “Static and dynamic behaviour of recycled tyre rubber-filled concrete.” *Cement and Concrete Research*, 32(10), 1587–1596.
- Hori, M., and Nemat-Nasser, S. (1993). “Double-inclusion model and overall moduli of multi-phase composites.” *Mechanics of Materials*, 14(3), 189–206.
- Hu, W. (2012). “Peridynamic models for dynamic brittle fracture.” *Engineering Mechanics Dissertations & Theses*.
- Jankowiak, T., and Lodygowski, T. (2005). “Identification of parameters of concrete damage plasticity constitutive model.” *Foundations of civil and environmental engineering*, 6(1), 53–69.
- Juenger, M. C. G., Winnefeld, F., Provis, J. L., and Ideker, J. H. (2011). “Advances in alternative cementitious binders.” *Cement and Concrete Research*, Conferences Special: Cement Hydration Kinetics and Modeling, Quebec City, 2009 & CONMOD10, Lausanne, 2010, 41(12), 1232–1243.
- Ke, Y., Beaucour, A. L., Ortola, S., Dumontet, H., and Cabrillac, R. (2009). “Influence of volume fraction and characteristics of lightweight aggregates on the mechanical properties of concrete.” *Construction and Building Materials*, 23(8), 2821–2828.
- Kim, H. K., Jeon, J. H., and Lee, H. K. (2012). “Workability, and mechanical, acoustic and thermal properties of lightweight aggregate concrete with a high volume of entrained air.” *Construction and Building Materials*, 29, 193–200.

- Kim, S.-M., and Abu Al-Rub, R. K. (2011). "Meso-scale computational modeling of the plastic-damage response of cementitious composites." *Cement and Concrete Research*, 41(3), 339–358.
- Li, S. (2008). "Boundary conditions for unit cells from periodic microstructures and their implications." *Composites Science and Technology*, 68(9), 1962–1974.
- Lubachevsky, B. D. (1991). "How to simulate billiards and similar systems." *Journal of Computational Physics*, 94(2), 255–283.
- Lubachevsky, B. D., and Stillinger, F. H. (1990). "Geometric properties of random disk packings." *Journal of statistical Physics*, 60(5–6), 561–583.
- Lubachevsky, B. D., Stillinger, F. H., and Pinson, E. N. (1991). "Disks vs. spheres: Contrasting properties of random packings." *Journal of Statistical Physics*, 64(3–4), 501–524.
- Lutz, M. P., Monteiro, P. J. M., and Zimmerman, R. W. (1997). "INHOMOGENEOUS INTERFACIAL TRANSITION ZONE MODEL FOR THE BULK MODULUS OF MORTAR." *Cement and Concrete Research*, 27(7), 1113–1122.
- Makarious, A. S., Bashter, I. I., El-Sayed Abdo, A., Samir Abdel Azim, M., and Kansouh, W. A. (1996). "On the utilization of heavy concrete for radiation shielding." *Annals of Nuclear Energy*, 23(3), 195–206.
- Meier, H. A., Kuhl, E., and Steinmann, P. (2008). "A note on the generation of periodic granular microstructures based on grain size distributions." *International journal for numerical and analytical methods in geomechanics*, 32(5), 509.
- Mori, T., and Tanaka, K. (1973). "Average stress in matrix and average elastic energy of materials with misfitting inclusions." *Acta Metallurgica*, 21(5), 571–574.
- Motamed, D., Milani, A. S., and others. (2013). "3D nonlinear XFEM simulation of delamination in unidirectional composite laminates: a sensitivity analysis of modeling parameters." *Open Journal of Composite Materials*, 3(04), 113.
- Nguyen, L. H., Beaucour, A.-L., Ortola, S., and Noumowé, A. (2014). "Influence of the volume fraction and the nature of fine lightweight aggregates on the thermal and mechanical properties of structural concrete." *Construction and Building Materials*, 51, 121–132.
- Nilsen, A. U., Monteiro, P. J. M., and Gjørv, O. E. (1995). "Estimation of the elastic moduli of lightweight aggregate." *Cement and Concrete Research*, 25(2), 276–280.
- Nunes, L. C. S., and Reis, J. M. L. (2012). "Estimation of crack-tip-opening displacement and crack extension of glass fiber reinforced polymer mortars using digital image correlation method." *Materials & Design*, 33, 248–253.
- Pan, B., Qian, K., Xie, H., and Asundi, A. (2009). "Two-dimensional digital image correlation for in-plane displacement and strain measurement: a review." *Measurement Science and Technology*, 20(6), 062001.
- Park, K., Paulino, G. H., and Roesler, J. (2010). "Cohesive fracture model for functionally graded fiber reinforced concrete." *Cement and Concrete Research*, 40(6), 956–965.
- Qian, Z., and Schlangen, H. (2013). "Lattice modeling of fracture processes in numerical concrete with irregular shape aggregates." *FraMCos-8: Proceedings of the 8th International Conference on Fracture Mechanics of Concrete and Concrete Structures, Toledo, Spain, 10-14 March 2013*, International Center for Numerical Methods in Engineering.
- Ravikumar, D., Peethamparan, S., and Neithalath, N. (2010). "Structure and strength of NaOH activated concretes containing fly ash or GGBFS as the sole binder." *Cement and Concrete Composites*, 32(6), 399–410.

- Ren, B., Wu, C. T., and Askari, E. (2017). "A 3D discontinuous Galerkin finite element method with the bond-based peridynamics model for dynamic brittle failure analysis." *International Journal of Impact Engineering*, 99, 14–25.
- Roesler, J., Paulino, G. H., Park, K., and Gaedcke, C. (2007). "Concrete fracture prediction using bilinear softening." *Cement and Concrete Composites*, 29(4), 300–312.
- Sancho, J. M., Planas, J., Cendón, D. A., Reyes, E., and Gálvez, J. C. (2007). "An embedded crack model for finite element analysis of concrete fracture." *Engineering Fracture Mechanics*, Fracture of Concrete Materials and Structures, 74(1–2), 75–86.
- Silling, S. A. (2000). "Reformulation of elasticity theory for discontinuities and long-range forces." *Journal of the Mechanics and Physics of Solids*, 48(1), 175–209.
- Silling, S. A., and Askari, E. (2005). "A meshfree method based on the peridynamic model of solid mechanics." *Computers & Structures*, Advances in Meshfree Methods, 83(17–18), 1526–1535.
- Silling, S. A., and Bobaru, F. (2005). "Peridynamic modeling of membranes and fibers." *International Journal of Non-Linear Mechanics*, Special Issue in Honour of C.O. Horgan, 40(2–3), 395–409.
- Silling, S. A., and Cox, J. V. (2014). "Hierarchical Multiscale Method Development for Peridynamics." *SAND Report*, 18565.
- Silling, S. A., Epton, M., Weckner, O., Xu, J., and Askari, E. (2007). "Peridynamic states and constitutive modeling." *Journal of Elasticity*, 88(2), 151–184.
- Silling, S. A., and Lehoucq, R. B. (2010). "Peridynamic Theory of Solid Mechanics." *Advances in Applied Mechanics*, Advances in Applied Mechanics, H. A. and E. van der Giessen, ed., Elsevier, 73–168.
- van der Sluis, O., Schreurs, P. J. G., Brekelmans, W. A. M., and Meijer, H. E. H. (2000). "Overall behaviour of heterogeneous elastoviscoplastic materials: effect of microstructural modelling." *Mechanics of Materials*, 32(8), 449–462.
- Song, S. H., Paulino, G. H., and Buttlar, W. G. (2006). "A bilinear cohesive zone model tailored for fracture of asphalt concrete considering viscoelastic bulk material." *Engineering Fracture Mechanics*, 73(18), 2829–2848.
- Suquet, P. (1987). "Elements of homogenization for inelastic solid mechanics."
- Thiele, A. M., Jamet, A., Sant, G., and Pilon, L. (2015). "Annual energy analysis of concrete containing phase change materials for building envelopes." *Energy Conversion and Management*, 103, 374–386.
- Voyatzis, G. Z., Taqieddin, Z. N., and Kattan, P. I. (2008). "Anisotropic damage–plasticity model for concrete." *International Journal of Plasticity*, 24(10), 1946–1965.
- Xia, Z., Zhou, C., Yong, Q., and Wang, X. (2006). "On selection of repeated unit cell model and application of unified periodic boundary conditions in micro-mechanical analysis of composites." *International Journal of Solids and Structures*, 43(2), 266–278.
- Yang, C. C. (1998). "Effect of the Transition Zone on the Elastic Moduli of Mortar." *Cement and Concrete Research*, 28(5), 727–736.
- Ye, C., Shi, J., and Cheng, G. J. (2012). "An eXtended Finite Element Method (XFEM) study on the effect of reinforcing particles on the crack propagation behavior in a metal–matrix composite." *International Journal of Fatigue*, 44, 151–156.
- Zanjani Zadeh, V., and Bobko, C. P. (2014). "Nanomechanical characteristics of lightweight aggregate concrete containing supplementary cementitious materials exposed to elevated temperature." *Construction and Building Materials*, 51, 198–206.

Preprint